50/5-13-92 JS (1)

PREPARED FOR THE U.S. DEPARTMENT OF ENERGY,
UNDER CONTRACT DE-AC02-76-CHO-3073

PPPL-2839
UC-420,427

PPPL-2839

TSC SIMULATION OF OHMIC DISCHARGES IN TFTR

BY

S.C. JARDIN, M.G. BELL, AND N. POMPHREY

April, 1992

PRINCETON
PLASMA PHYSICS
LABORATORY

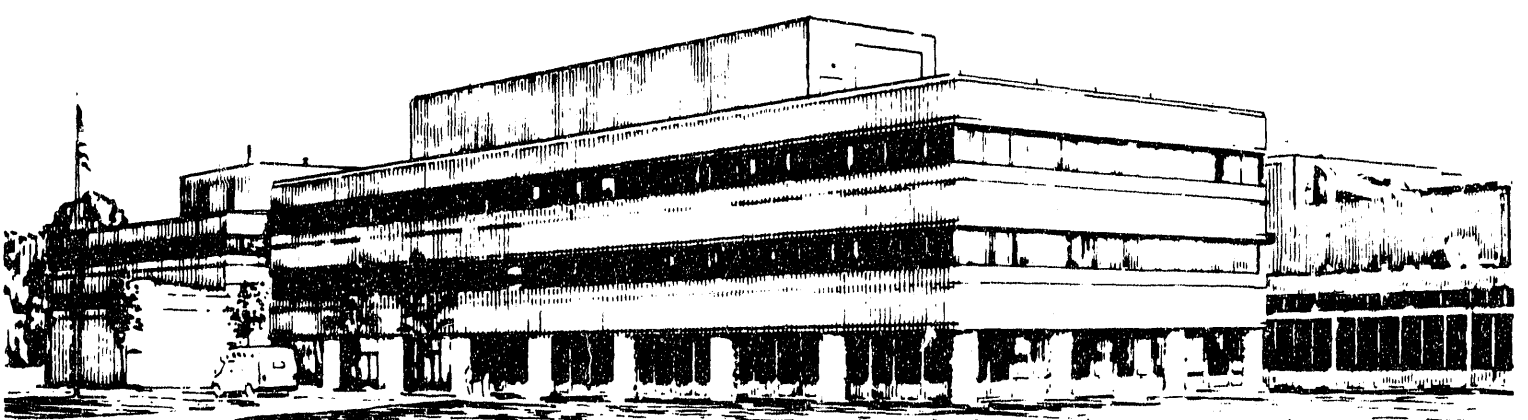

DISTRIBUTION OF THIS DOCUMENT IS UNLIMITED

NOTICE

This report was prepared as an account of work sponsored by an agency of the United States Government. Neither the United States Government nor any agency thereof, nor any of their employees, makes any warranty, express or implied, or assumes anv legal liability or responsibility for the accuracy, completeness, or usefulness of any information, apparatus, product, or process disclosed, or represents that its use would not infringe privately owned rights. Reference herein to any specific commercial produce, process, or service by trade name, trademark, manufacturer, or otherwise, does not necessarily constitute or imply its endorsement, recommendation, or favoring by the United States Government or any agency thereof. The views and opinions of authors expressed herein do not necessarily state or reflect those of the United States Government or any agency thereof.

NOTICE

This report has been reproduced directly from the best available copy.

Available to DOE and DOE contractors from the:

Office of Scientific and Technical Information
P.O. Box 62
Oak Ridge, TN 37831;
Prices available from (615) 576-8401.

Available to the public from the:

National Technical Information Service
U.S. Department of Commerce
5285 Port Royal Road
Springfield, Virginia 22161
703-487-4650

TSC Simulation of Ohmic Discharges in TFTR

PPPL--2839

DE92 013249

S. C. Jardin, M. G Bell, and N. Pomphrey

Princeton University

Plasma Physics Laboratory

P.O. Box 451

Princeton, NJ 08543

Abstract

The Tokamak Simulation Code (TSC) has been used to model the time dependence of several ohmic discharges in the TFTR experiment. We have refined the semi-empirical thermal conductivity model and the sawtooth model in TSC so that good agreement is obtained between the simulation and the experiment in electron and ion temperature profiles, and in the current profiles for the entire duration of the discharges. Neoclassical resistivity gives good agreement with the measured surface voltages and rate of poloidal flux consumption.

MASTER

1. Introduction

The Tokamak Simulation Code[1] (TSC) is a two-dimensional time dependent free boundary simulation code that advances the MHD equations describing transport time scale evolution of an axisymmetric magnetized tokamak plasma. TSC evolves the magnetic field in a rectangular computational domain using the Maxwell MHD equations for the plasma, coupled through boundary conditions to the circuit equations for the tokamak poloidal field (PF) coils. The plasma model in TSC is completed by providing functional forms for the electron and ion thermal conductivities, for the particle diffusion coefficients, and for the plasma electrical resistivity.

A semi-empirical plasma transport model[2-6], is presently utilized in TSC. While having some theoretical and empirical foundations, the model contains several free coefficients, or adjustable parameters, which are chosen so that the predictions of the simulation code agree as closely as possible with the experimental data base. We report here on our experience in benchmarking or calibrating this model against ohmic discharges in the TFTR experiment.

2. The TSC Model

TSC solves a modified force balance equation on a background Cartesian grid to maintain the plasma in near equilibrium during its evolution.[1] The poloidal flux function, Ψ, and the toroidal field function, g, are also evolved on this fixed background grid, where the axisymmetric magnetic field is represented in the standard form.

$$\vec{B} = \nabla\phi \times \nabla\Psi + g\nabla\phi \quad , \tag{1}$$

with ϕ being the symmetry angle in a cylindrical coordinate system (R, ϕ, z).

The evolving magnetic surfaces define a magnetic geometry which changes in time. We use the toroidal flux inside a magnetic surface Φ as the coordinate label for that surface. The large ratios of parallel to perpendicular diffusivity and parallel to perpendicular thermal conductivity allow magnetic surface averaging to obtain one-dimensional transport equations for number and entropy densities,

where time derivatives are with respect to surfaces containing fixed toroidal flux:[7,8].

$$\frac{\partial}{\partial t} N' = -\frac{\partial}{\partial \Phi}\left(N'\Gamma\right) + S_N \tag{2}$$

$$\frac{\partial}{\partial t}\sigma = \frac{2}{3}\left(\frac{\partial V}{\partial \Phi}\right)^{2/3}\left[V_L\frac{\partial K}{\partial \Phi} - \frac{\partial}{\partial \Phi}(Q_i + Q_e) + \frac{\partial V}{\partial \Phi}\left(S_e + S_i - R_e\right)\right] \tag{3}$$

$$\frac{\partial}{\partial t}\sigma_e = \frac{2}{3}\left(\frac{\partial V}{\partial \Phi}\right)^{2/3}\left[V_L\frac{\partial K}{\partial \Phi} - \frac{\partial Q_e}{\partial \Phi} + \frac{\partial V}{\partial \Phi}\left(-\Gamma\frac{\partial p_i}{\partial \Phi} + Q_{\Delta e} + S_e - R_e\right)\right] \tag{4}$$

In Equ's (2) – (4), the quantities being advanced in time are the differential electron number density $N' = n_e \partial V/\partial \Phi$, and the differential total and electron entropy densities $\sigma = p\left(\partial V/\partial \Phi\right)^{5/3}$ and $\sigma_e = p_e\left(\partial V/\partial \Phi\right)^{5/3}$. The derivative, $\partial V/\partial \Phi$, is the differential volume element

$$\frac{\partial V}{\partial \Phi} = \frac{\partial}{\partial \Phi}\oint d\tau = \frac{1}{q}\oint \frac{d\ell}{Bp} \tag{5}$$

and p, p_e are the total and electron pressures. Also,

$$V_L = \frac{2\pi\left\langle \vec{E}\cdot\vec{B}\right\rangle}{\left\langle B\cdot\nabla\phi\right\rangle} \tag{6}$$

is the loop voltage, and

$$K = \oint \vec{B}_p\cdot d\ell = \oint \frac{d\ell\left|\nabla\Psi\right|}{R} \tag{7}$$

is the total toroidal current within a flux surface.

Electron and ion heat fluxes are defined as

$$Q_i = \frac{\partial V}{\partial \Phi}\left(\langle \vec{q}_i \cdot \nabla \Phi \rangle + \frac{5}{2} p_i \Gamma\right) \tag{8}$$

$$Q_e = \frac{\partial V}{\partial \Phi}\left(\langle \vec{q}_e \cdot \nabla \Phi \rangle + \frac{5}{2} p_e \Gamma\right) \quad , \tag{9}$$

where $\vec{q}_e$ and $\vec{q}_i$ are the random heat flux vectors, Γ denotes particle flux, and the standard definition of flux surface average operator is used:

$$\langle a \rangle = \frac{\oint (d\ell/B_p) a}{\oint (d\ell/B_p)} \quad .$$

The plasma is assumed to have two temperatures; T_e for the electrons of density n_e, and T_i for the temperature of the bulk ions of charge Z_i, mass M_i, and density n_i. A single impurity ion is assumed of charge Z_I, mass M_I and density n_I.

Pressures, densities, and temperatures are related in the standard way,

$$k_B T_e = p_e / n_e \quad , \tag{10}$$

$$k_B T_i = p_i / (n_i + n_I) \quad , \tag{11}$$

with $k_B = 1.60 \times 10^{-19}$(J/eV). Also, from charge neutrality, we have

$$n_e = Z_i n_i + Z_I n_i \quad . \tag{12}$$

The effective charge, $\overline{Z}$, and the equipartition charge, $< Z >$, are defined as

$$\overline{Z} = \left(n_i Z_i^2 + n_I Z_I^2\right) / n_e \quad , \tag{13}$$

and

$$\langle Z \rangle = \left(n_i Z_i^2 / M_i + n_I Z_I^2 / M_I\right) / (n_e / M_H) \quad , \tag{14}$$

where M_H is the proton mass.

2.1 Resistivity and Equipartition

The equipartition term appearing in Eq. (4) is given by [9]

$$Q_{\Delta e} = \frac{3}{2}\left[p_i - \frac{(n_i + n_I)}{n_e} p_e\right] / \tau_{\Delta e} \tag{15}$$

where

$$\tau_{\Delta e}^{-1} = 3.1 \times 10^{-11}\, n_e\left[m^{-3}\right] \eta_c\left[\Omega m\right] \langle Z \rangle\, s^{-1} \quad ,$$

and η_c is the classical plasma resistivity for a hydrogen plasma, given by [9]

$$\eta_c = \left(1.03 \times 10^{-4}\right) \ell n\Lambda \left[T_e\,(eV)\right]^{-3/2} \Omega m \quad , \tag{16}$$

with

$$\ell n\Lambda = 17.1 - \ell n \left\{\left[n_e(m^{-3})\right]^{1/2} \left[T_e(eV)\right]^{-1}\right\} \quad .$$

Neoclassical corrections to the resistivity are assumed. These are given by [10]

$$(\eta_c / \eta_{NC}) = \Lambda_E(\overline{Z}) \left(1 - \frac{f_t}{1 + \xi(\overline{Z})\nu_{*e}}\right)\left(1 - \frac{C_R(\overline{Z})\, f_t}{1 + \xi(\overline{Z})\nu_{*e}}\right) \quad , \tag{17}$$

where

$$\Lambda_E(\overline{Z}) = \frac{3.40}{\overline{Z}}\left(\frac{1.13 + \overline{Z}}{2.67 + \overline{Z}}\right) \quad ,$$

$$C_R(\overline{Z}) = \frac{0.56}{\overline{Z}}\left(\frac{3.0 - \overline{Z}}{3.0 + \overline{Z}}\right) \quad ,$$

$$\xi(\overline{Z}) = 0.58 + 0.20\,\overline{Z} \quad ,$$

and the electron collisionality parameter is evaluated as

$$\nu_{*e} = \left(10.2 \times 10^{16}\right) R_o[m]\, q\, n_e(m^{-3})\, \Lambda / \left(f_t\, \delta\, [T_e(eV)]^2\right) \quad .$$

Here, the local inverse aspect ratio is evaluated as $\delta = a/R_o$ where

$$a = \left[V/\left(2\pi^2 R_o\right)\right]^{1/2} \quad ,$$

V is the volume inside a given magnetic surface, and R_o is the radius of the magnetic axis. The trapped particle fraction, f_t, is evaluated in terms of surface averages over the magnetic surfaces as follows[7]

$$f_t = 1 + \langle B^2\rangle\langle B^{-2}\rangle + \frac{3}{2}\langle B^2\rangle\left\langle B^{-2}\left[\left(1 - B/B_c\right)^{1/2} - \frac{1}{3}\left(1 - B/B_c\right)^{3/2}\right]\right\rangle \quad , \tag{18}$$

where B_c is the maximum value of $|\vec{B}|$ on a given flux surface.

In the absence of other forms of current drive, the parallel electric field is the sum of two terms, the resistive diffusion term and the bootstrap current drive term. Thus,

$$\vec{E}\cdot\vec{B} = \eta_{\parallel}\left[\vec{J}\cdot\vec{B} - \vec{J}_{BS}\cdot\vec{B}\right] \quad . \tag{19}$$

Here

$$\vec{J} = \mu_o^{-1}\, \nabla \times \vec{B} \tag{20}$$

is the total current density, and $\vec{J}_{BS}$ is the bootstrap current density given by [11]

$$\vec{J}_{BS}\cdot\vec{B} = -g\, p_e\left\{N_1\left[p_e'/p_e + \frac{1}{\overline{Z}}\frac{p_i}{p_e}\left(\frac{p_i'}{p_i} + \alpha_i\frac{T_i'}{T_i}\right)\right] - N_2\, T_e'/T_e\right\}/D \quad . \tag{21}$$

Here

$$N_1 = f_x\left(0.754 + 2.21\,\overline{Z} + \overline{Z}^2\right) + f_x^2\left(0.348 + 1.24\,\overline{Z} + \overline{Z}^2\right) \quad ,$$

$$N_2 = f_x\left(0.884 + 2.07\,\overline{Z}\right) \quad ,$$

$$D = 1.414\,\overline{Z} + \overline{Z}^2 + f_x\left(0.754 + 2.657\,\overline{Z} + 2\overline{Z}^2\right) + f_x^2\left(0.348 + 1.243\,\overline{Z} + \overline{Z}^2\right) \quad ,$$

$$\alpha_i = -1.172/(1.0 + 0.462\,f_x) \quad ,$$

$$f_x = f_t/\left(1 - f_t\right) \quad .$$

A simple modification of the neoclassical resistivity has been used in the calculations presented here to take into account the effect of the sawtooth instability on the evolution of the plasma. Sawtoothing models exist which attempt to resolve in time the occurrence of each sawtooth event[13]. Rather than incorporate one of these, which would necessitate resolving the evolution of the equilibrium on the rapid time scale of the sawtooth period and crash, we utilize a time average model which consists of enhancing the resistivity inside the magnetic surface where $q = 1$. We introduce a parameter $0 < a_{120} \leq 1$ which represents the degree which the resistivity profile, and hence the steady state current profile, is flattened interior to the sawtooth inversion radius. In terms of this parameter, the sawtooth model can be described as

$$\eta_{\parallel} = \eta_{NC} \qquad \text{for } q \geq 1 \tag{22}$$

$$\eta_{\parallel} = a_{120}\,\eta_{NC} + (1 - a_{120})\,\eta_{NC}(q = 1) \qquad \text{for } q < 1 \quad .$$

2.2 Thermal Conductivity

The random heat flux contributions to Q_i and Q_e in equations (8) and (9) are evaluated using a general geometry formulation of the Coppi-Tang transport model. This has the electron and the ion heat fluxes each depending only on their own respective temperature gradients. Thus, the random heat fluxes are of the form

$$\langle \vec{q}_i \cdot \nabla \Phi \rangle = -\chi_i |\nabla \Phi|^2 n_i \frac{\partial T_i}{\partial \Phi} \quad , \tag{23a}$$

$$\langle \vec{q}_e \cdot \nabla \Phi \rangle = -\chi_e |\nabla \Phi|^2 n_e \frac{\partial T_e}{\partial \Phi} \quad . \tag{23b}$$

The electron and ion thermal conductivities are taken to be of the following form[6]

$$|\nabla \Phi|^2 \chi_e = f_m \left(\chi_{TE,1}^2 + \chi_{\eta i}^2\right)^{1/2} F(\Phi) \quad , \tag{24}$$

$$\chi_i = a_{126}\, \chi_e \tag{25}$$

where a_{126} is a constant parameter, and $F(\Phi)$ is a profile factor given by

$$F(\Phi) = 8\pi^2 \frac{P(\Phi)}{P(\Phi_o)} \frac{n_e(0)}{n_e(\Phi)} \frac{R_o \Phi_o}{(\partial V/\partial \Phi)} \exp\left[2/3\, \alpha_q \Phi / \Phi_o\right] . \tag{26}$$

Here Φ_o is equal to the toroidal flux Φ at the plasma boundary, $P(\Phi)$ is the total heating power (including ohmic heating) minus the total radiated power inside surface Φ, and α_q is taken to be

$$\alpha_q = q_{95} + 0.5 \quad , \tag{27}$$

where q_{95} is the safety factor at the surface containing 95% of the toroidal flux between the magnetic axis and the plasma edge. We limit α_q to lie between 2.5 and 6.5 to avoid unphysical results in regimes where the assumptions underlying the transport model presented here are not valid.

The functional form of the profile factor $F(\Phi)$ given in Eq. (26) follows from the insertion of the empirical steady state temperature profile

$$T(\Phi)/T(0) = \exp\left[-2/3\, \alpha_q\, \Phi / \Phi_o\right]$$

into the steady form of Eq. (3), and using the definitions in Eq. (8), (9), (23) to solve for χ_e and χ_i. It is an arbitrary geometry generalization of the form first suggested by Coppi.[2]

From Ref. [3] we obtain multipliers for the two confinement regimes

$$\chi_{TEM} = a_{122}\, 1.25 \times 10^{20} \frac{a}{n(\Phi_o)} (RB_T)^{0.3}\, \overline{Z}^{\,0.2} \left(1 + \frac{1}{4}\alpha_n\right) R^{-2.2} q_{95}^{-1.6} \quad , \tag{28}$$

$$\chi_{\eta i} = a_{121}\, 7.5 \times 10^{8} \left[\frac{P(\Phi_o)}{n(\Phi_o)}\right]^{0.6} (RB_T q_{95})^{-0.8} a^{-0.2} \quad . \tag{29}$$

These are combined in accordance with Eq. (24).

The factor f_m in Eq. (24) is used to account for the time averaged effect of the sawtooth instability in causing additional flattening of the temperature profile inside the q = 1 surface. Thus, in addition to the prescription given in Eq. (22) for modifying the resistivity profile, the sawtooth model is completed by enhancing the thermal conductivity interior to the sawtooth inversion radius according to the prescription

$$\begin{aligned} f_m &= 1 \qquad \text{for } q > 1 \\ f_m &= a_{124} \qquad \text{for } q > 1 \quad . \end{aligned} \tag{30}$$

2.3 Particle Transport

In all of the simulations presented below, the particle flux Γ appearing in Eqs. (2), (4), (8), and (9) was set to zero

$$\Gamma = 0 \quad . \tag{31}$$

The source term S_N in Eq. (2) was continuously adjusted so that the electron density profile $n_e(\Phi)$ match both the experimentally measured line averaged density and central density, where the experimental data was digitized every

0.0002 seconds. This matching was achieved by assuming a density profile of the form

$$n_e(\phi,t) = n_e^o(t)\left[1 - \tilde{\Psi}^{\beta_N}\right]^{\alpha_N(t)} + n_b(t) \tag{32}$$

where $\tilde{\Psi}$ is the normalized poloidal flux which varies between 0 at the magnetic axis and 1 at the plasma boundary, and $n_b(t)$ is the density at the plasma boundary. In these studies, we set $\beta_N = 1.0$, $n_b = (0.1)\, n_e^o$ and adjusted $n_e^o(t)$ and $\alpha_N(t)$ to match the experimental data.

This approach for modeling the density evolution was adopted for several reasons. One is that we are unaware of a satisfactory dynamic particle transport model for the density profile. Even if such a model did exist, it would be very difficult to infer the actual source S_N in the presence of both gas fueling and recycling under actual conditions. Note that the derivation used in obtaining the thermal conductivity form factor, Eq. (26), assumed that $\Gamma = 0$, so that these two assumptions are consistent.

2.4 Radiation and Impurities

In the simulations reported, it was assumed that the dominant radiation was from fully stripped ions. The surface averaged radiated power density is computed as[14]

$$R_e(\Phi,t) = 1.7 \times 10^{-38}\left[n_e(\Phi,t)(m^{-3})\right]^2 \bar{Z}(t)\left[T_e(\Phi,t)(eV)\right]^{1/2} \quad . \tag{33}$$

The variation of the effective charge with time, $\bar{Z}(t)$, was computed from visible Bremsstrahlung, assuming the radial dependence to be flat. Taking the dominant impurity to be carbon, $Z_I = 6$, defines the ratio of impurity to ion density n_I/n_i from Eq. (14).

2.5 Boundary Conditions

The boundary conditions required for TSC are of two kinds:

(i) electromagnetic boundary conditions needed to evolve the magnetic field and hence define the magnetic geometry, and (ii) transport boundary conditions for the surface average densities and temperatures.

The magnetic boundary conditions are largely defined by using the experimentally measured currents in the four coil systems in TFTR; the ohmic heating system $I_{OH}(t)$, the equilibrium field system $I_{EF}(t)$, the variable curvature field system $I_{VC}(t)$, and the toroidal field system $I_{TF}(t)$. The coordinates of each of the polodial field coils in these groups is listed in Table I.

The experimental currents were modified in two ways for the simulations reported here. A plasma current control feedback system was used in the simulation in which a fictitious loop voltage $V_f(t)$ was added to the computational boundary each time step to force the plasma current in the simulation to match the experimental plasma current. The time integral of this, $\Delta\Psi_s^{PF} = \int V_f(t)\,dt$, represents the error of the simulation in reproducing the experimental volt second consumption.

A similar feedback system was used in the simulation to add a small correction to the equilibrium field system current $I_{EF}(t)$, to force the plasma major radius in the simulation to match the experimental value $R_p(t)$. Again, this feedback correction, $\delta I_{EF}(t)$, is a measure of the error in the simulation.

The TFTR limiters can be represented by two circular arc segments, an inner one with major radius R = 2.661 m, minor radius a = 1.01 m, and extending for 1.047 radians, and an outer one with R = 2.601 m, a = 0.990 m, and extending for 2.043 radians. We define the plasma boundary as being the innermost magnetic flux surface that makes contact with one of these limiter surfaces. At the plasma boundary we apply the boundary condition that the electron density is 30% of its central value, and that both the electron and ion temperatures are equal to the "vacuum temperature", an input variable for TSC which we set to between 2 and 4 electron volts.

2.6 Free Parameters

In the simulation model there are five free parameters which are best determined by calibrating the simulation results to experimental data. These parameters, and the equation numbers where they were introduced, are a_{122}(25), which describes resisivity flattening inside the q = 1 surface; a_{126}(25), the ratio of ion to electron thermal conductivity; a_{122}(28) and a_{121}(29), coefficients for the TEM and η_i induced transport; and a_{124}(30)which describes the additional flattening of the temperature profile inside the q = 1 surface

In all the simulations presented here, we have used the following values for these parameters

$$
\begin{aligned}
a_{120} &= 0.10 \\
a_{121} &= 0.08 \\
a_{122} &= 0.40 \\
a_{124} &= 4.00 \\
a_{126} &= 1.00
\end{aligned}
\tag{34}
$$

3.0 Experimental Comparisons

We report here on the success of the TSC simulation model described in Section 2 in reproducing the time dependence of 7 ohmically heated helium discharges in TFTR. These discharges, which ranged in peak plasma current from 1.0 to 2.2 MA and in central density from 0.30 to 0.70 x 10^{20} m^{-3}, were all used in the parallel resistivity study reported in Reference [15]. Their parameters are listed in Table II.

The evolution of the plasma current, I_p, and major radius, R, for Shot 24095 is shown in Fig. 1. (The evolution of the other six shots considered here is qualitatively similar.) The simulation time ranges from 0.05 to 4.50 sec after plasma initiation. The plasma current was ramped at approximately 3.0 to 5.0 MA/sec, until it reached a value of 1 MA, at which point the ramp rate was decreased to about 0.5 MA/sec until the current reaches its flattop value. The 1.0 MA/sec current rampdown begins at 3.5 sec.

As indicated by Fig. 1., the plasma is grown off the outer limiter. During the current rampup the minor radius increases from 0.60 m to 0.83 m.

Figure 2 shows the experimentally measured and the simulation values for the effective charge $Z_{eff}(t)$, the line averaged density $\bar{n}_e(t)$, and the ratio of peak to volume average density $n_e^o/\langle n_e\rangle(t)$. These quantities were input into the simulation as discussed in Sections 2.3 and 2.4. The slight differences between the simulation and the experimental curves are an artifact of the way in which this data was input into the simulation: the values of $Z_{eff}(t)$ and the density exponent $\alpha_N(t)$, were taken as piecewise linear over 0.5 sec intervals, whereas the line averaged interval was 2 ms.

The results of this simulation, together with the corresponding experimental data, is shown in Figs. 3 through 9. Figs. 3 and 4 show the time history of both the electron and ion central temperatures and their peak to average ratios. Both the central electron and ion temperatures in the simulation are seen to track the experimental values to within 10% for the entire duration of the simulation.

Figures 3b and 4b show the TSC transport model is capable of tracking not only the central temperatures, but to a large degree, the temperature profiles during the current rampup. Although slightly overestimating the peakedness of the profiles during the initial second of current rise, the model correctly reproduces the time at which the profiles peak ($t \approx 1.2$ s) and the time at which they become most broad ($t \approx 3.5$ s), and quite accurately reproduces the profile shape during the interval in between. A comparison of the temperature and density profiles across the midplane at the end of the current flattop, $t = 3.5$ sec, is given in Fig. 5.

In Fig. 6 we plot a comparison of the total volt-seconds delivered to the plasma in the experiment (E) and the simulation (S), as well as a breakdown of the resistive (R) and internal (I) components in the simulation. Here, the experimental curve is computed directly from the coil currents as the total flux linkage from all coils to the nominal plasma center at $R_p = 2.65$, $Z_p = 0$. Thus, if

M_{pi} is the mutual inductance between coil i and the plasma, the experimental volt-seconds is computed as

$$E = \sum_{i=1}^{N} M_{pi} \Delta I_i \quad ,$$

Where ΔI_i is the amount that the current in coil i has changed since the simulation began (t = 0.05 sec). The total volt-seconds used in the simulation is computed as

$$S = \sum_{i=1}^{N} M_{pi} \Delta I_i + \Delta \Psi_s^{PF} \quad ,$$

where $\Delta \Psi_s$ is the time integral of the additional fictitious loop voltage used in the simulation.

Also plotted in Fig. 6 is the resistive volt-second consumption in the simulation, defined as the time integral of the loop voltage on the plasma magnetic axis,[16] or as the change of poloidal flux there. Thus,

$$R = \Delta \Psi_{axis}^{PF} = \int_0^t \eta_{\parallel}(0)\, J(0)\, dt$$

Where the second equality follows from application of Faraday's law and Ohm's law Eq. (19). The internal volt second curve is the change in poloidal flux at the plasma limiter

$$I = \Delta \Psi_{limiter}^{PF} \quad .$$

Thus, the difference between the curves marked I and R is the total poloidal flux difference between the limiter and the magnetic axis at a given time.

Figures 7 and 8 show a comparison between the simulation and the experimental values of $\Lambda = \ell_i /2 + \beta_p$, and of the currents in the equilibrium field

coils, I_{EF}. The experimental curve for Λ was determined purely from magnetics measurements using the Shafranov formula. The simulation curve was calculated from computing integrals over the plasma volume using the definitions

$$\ell_i = \frac{2}{R_p \mu_o^2 I_p^2} \int B_p^2 dV \quad ,$$

$$B_p = \frac{4}{R_p \mu_o I_p^2} \int P \, dV \quad .$$

Note that the simulation current in the equilibrium field coils system is the sum of the experimental value and the feedback correction as discussed in Section 2.5,

$$I_{EF}^{Sim}(t) = I_{EF}^{Exp}(t) + \delta I_{EF}(t) \quad .$$

Finally, in Fig. 9 we show a comparison between the radius of the q = 1 surface as computed in the simulation and as deduced experimentally by the soft x-ray camera.

Table II summarizes the results from all 7 simulations, and the comparisons with the corresponding discharges. For each, we list the total volt-seconds required for the 4.5 seconds of simulation time, the axial resistive volt-second consumption in the simulation, and the difference between the experimental and simulation volt-second consumption $\Delta\Psi_s^{PF}$. We also list the maximum electron and ion temperatures that occurred in the simulation and the experiment. The simulation temperatures are seen to be generally within 10% of the experimental values, over the range of discharges.

The amount of resistive volt-seconds consumed in these different discharges was remarkably similar, all falling within the narrow range from 3.2 to 3.6. The total volt-seconds required ranged from 11.3 for the 1.0 MA discharge to 16.4 for a 2.2 MA discharge. The absolute error in the volt-second consumption ranged from −0.3 to 0.5. This amounts to a maximum error of 4% in the total volt-seconds consumed, or an error of 15% in the resistive component.

4.0 Discussion and Summary

The primary intent of this paper was to demonstrate that the plasma model which has been incorporated into the TSC code can reproduce many of the features of a tokamak discharge to an accuracy close to the experimental uncertainty. These features include peak and average temperatures, current profile evolution, location of the sawtooth inversion radius, and volt-second consumption. This gives us some confidence for using TSC as a design tool for future experiments.

In performing the calibration runs presented here, there were several interesting trends noted which are outside of the original scope of this paper but which deserve mention. Probably the most important of these is that no anomalous parallel resistivity was needed to reproduce the current evolution and volt-second consumption in TFTR, even during the current rampup phase. This has been reported previously[15] but is confirmed by the present study.

A second observation of interest is on the evolution of the peak to average temperature profile as illustrated in Fig. 3b. It is seen that this ratio reaches a maximum during the current ramp at 1.1 sec, which is the time when the plasma minor radius has grown to its full value (see Fig. 1). The ratio then decreases steadily until about 3.5 sec when the current ramp down begins. This long timescale is apparently set by the current diffusion time. It has also been noted in previous publications.[17]

It may well be possible to exploit this temperature profile evolution effect in a transient ignition experiment such as the proposed BPX[18] and IGNITOR[19] devices. The more peaked the temperature profiles, the easier it is to satisfy the ignition criteria for a DT tokamak. By timing the current ramp and shape evolution of the discharge properly, it may well be possible to ignite the tokamak before the temperature profile broadening begins.

Acknowledgements

This work was supported by US Department of Energy contract number DE-AC02-76-CHO3073.

Figure Captions

Figure 1 (a) Plasma current and (b) major radius vs. time. Comparison of TSC simulation (———) and experimental data (·····) (agreement aided by feedback on OH and EF systems as explained in Section 2.5.)

Figure 2 Experimentally measured (·····) and simulation curves (———) for (a) the effective charge $Z_{eff}(t)$, (b) the line averaged density $\bar{n}_e(t)$ and (c) the ratio of peak to average density $n_e^o / \langle n_e \rangle (t)$. These were input into the simulation as discussed in Sections 2.3 and 2.4

Figure 3 Time history of simulation (———) and experimental values (·····) of (a) central electron temperature and (b) ratio of peak to average electron temperature

Figure 4 Time history of simulation (———)and experimental values (·····) of (a) central ion temperature and (b) ratio of peak to average values of ion temperature

Figure 5 Comparison of the simulation (———) and experimental values (·····) of (a) electron temperature, (b) ion temperature and (c) electron density vs. minor radius at t = 3.5 sec.

Figure 6 Comparison of the total volt-seconds delivered to the plasma in the experiment (·····) and simulation (———). Also shown is the breakdown in the simulation between internal (I) and resistive (R) using "axial" accounting

Figure 7 Coil currents vs. time for the three coil systems for the simulation (———) and experiment (·····). I_{EF} is the equilibrium field system, I_{OH} is the ohmic heating system, and I_{VC} is the variable curvature system. The latter two were the same for the simulation and the experiment

Figure 8 Comparison between the simulation (———) and the experimental (·····) values of $\Lambda = \ell_i / 2 + \beta_p$. Experimental curve is from magnetics measurements.

Figure 9 Comparison between the radius of the q = 1 surface in the simulation, (———) and the value deduced experimentally (·····).

TABLE I

TFTR PF COILS

R(m)	Z(m)	Turns	ΔR(m)	ΔZ(m)
OH Coils				
0.6668	0.2451	100	0.1924	0.4070
0.6703	0.7688	40	0.1721	0.1992
0.7797	0.8020	7	0.0486	0.1328
0.8162	0.8351	2	0.0243	0.0664
0.7551	1.0133	71	0.2576	0.2162
0.9108	0.9863	4	0.0566	0.0541
0.9250	1.0673	11	0.0850	0.1081
0.9816	1.0943	2	0.0283	0.0541
1.1980	1.5861	26	0.1706	0.1717
1.6040	1.8424	18	0.1433	0.1580
2.3324	2.1380	9	0.0592	0.1547
2.8390	2.3040	5	0.1217	0.0462
3.8798	2.0860	6	0.1549	0.0655
4.9997	0.7101	2	0.0372	0.0696
EF Coils				
2.8403	2.1694	-9	0.1028	0.1550
3.8785	1.9471	-14	0.1547	0.1560
4.8809	0.8088	-26	0.1467	0.3428
VC Coils				
0.7170	1.4650	27	0.1220	0.2339
1.6046	2.0202	-15	0.1269	0.1443
2.3326	2.2959	-4	0.0503	0.0888
4.9997	0.8748	3	0.0372	0.1090

TABLE II

RESULTS SUMMARY .05 $\leq t \leq$ 4.5 SEC

SHOT	I_p^{MAX} MA	$n_e^o \times 10^{14}$ m^{-3}	V-SEC TOT	V-SEC RES	$\Delta\Psi_s^{PF}$	MAX (KeV) $T_{e(o)}^{EXP}$	MAX (KeV) $T_{e(o)}^{SIM}$	MAX (KeV) $T_{i(o)}^{EXP}$	MAX (KeV) $T_{i(o)}^{SIM}$
24088	2.2	.35	16.2	3.4	.01	4.4	4.4	2.9	3.4
24095	2.2	.35	16.1	3.6	-.10	4.4	4.5	3.0	2.9
24096	2.2	.65	16.4	3.4	-.12	3.8	3.5	3.0	3.0
24098	1.8	.30	14.2	3.4	.06	4.5	4.2	3.1	3.1
24100	1.8	.70	14.2	3.3	-.33	4.0	3.6	3.2	2.9
24093	1.4	.37	12.3	3.2	.45	3.4	3.4	2.7	2.7
24089	1.0	.66	11.3	3.4	-.20	2.5	2.8	2.2	2.3

REFERENCES

1. S. C. Jardin, N. Pomphrey, J. L. DeLucia, J. Comput. Phys. 66 481 (1986).

2. B. Coppi, Comm. Plasma Phys. Controll. Fusion 5 261 (1980).

3. W. M. Tang, Nucl. Fusion 26 1605 (1986).

4. M. H. Redi, W. M. Tang, P. C. Efthimion, et al., Nucl. Fusion 27 2001 (1987).

5. V. Arunasalam, N. L. Bretz, P. C. Efthimion, et al., "On the Self-Consistency of the Principle of Profile Consistency Results for Sawtoothing Tokamak Discharges," Princeton Plasma Physics Laboratory Report, PPPL-2609, May 1989.

6. S. C. Jardin, J. DeLucia, M. Okabayashi, et al., Nucl. Fusion 27 569 (1987).

7. S. P. Hirshman, S. C. Jardin, Phys. Fluids 22 731 (1979).

8. S. C. Jardin, J. of Comput. Phys. 43 31 (1980).

9. D. L. Book, "NRL Plasma Formulary," NRL Publication 0084-4040 (1987).

10. S. P. Hirshman, R. J. Hawyluk, B. Birge, Nucl. Fusion 17 611 (1977).

11. S. P. Hirshman, Phys. Fluids 31 3150 (1988).

12. B. B. Kadomtsev, Soc. J. Plasma Phys. 1 389 (1975).

13. D. J. Ward and S. C. Jardin, Nucl. Fusion 29 905 (1989).

14. J. Sheffield, "Tokamak Startup," H. Knoepfel, Editor, Plenum Press.

15. M. C. Zarnstorff, K. McGuide, M. G. Bell, et al., Phys. Fluids B 2 1852 (1990).

16. R. J. Hawryluk and J. A. Schmidt, Nucl. Fusion 16 775 (1976).

17. E. D. Fredrickson, K. M. McGuire, R. J. Goldston, et al., Nucl. Fusion 27 1897 (1987).

18. S. C. Jardin, "Physics Overview of CIT," Paper 26-I-01, in Proceedings of 13th Symposium on Fusion Engineering, Knoxville, TN (1989).

19. B. Coppi and the Ignitor Program Group, in Plasma Physics and Controlled Nuclear Fusion Research, 1988, IAEA (Nice, October 1988) Vo. 3, p. 357.

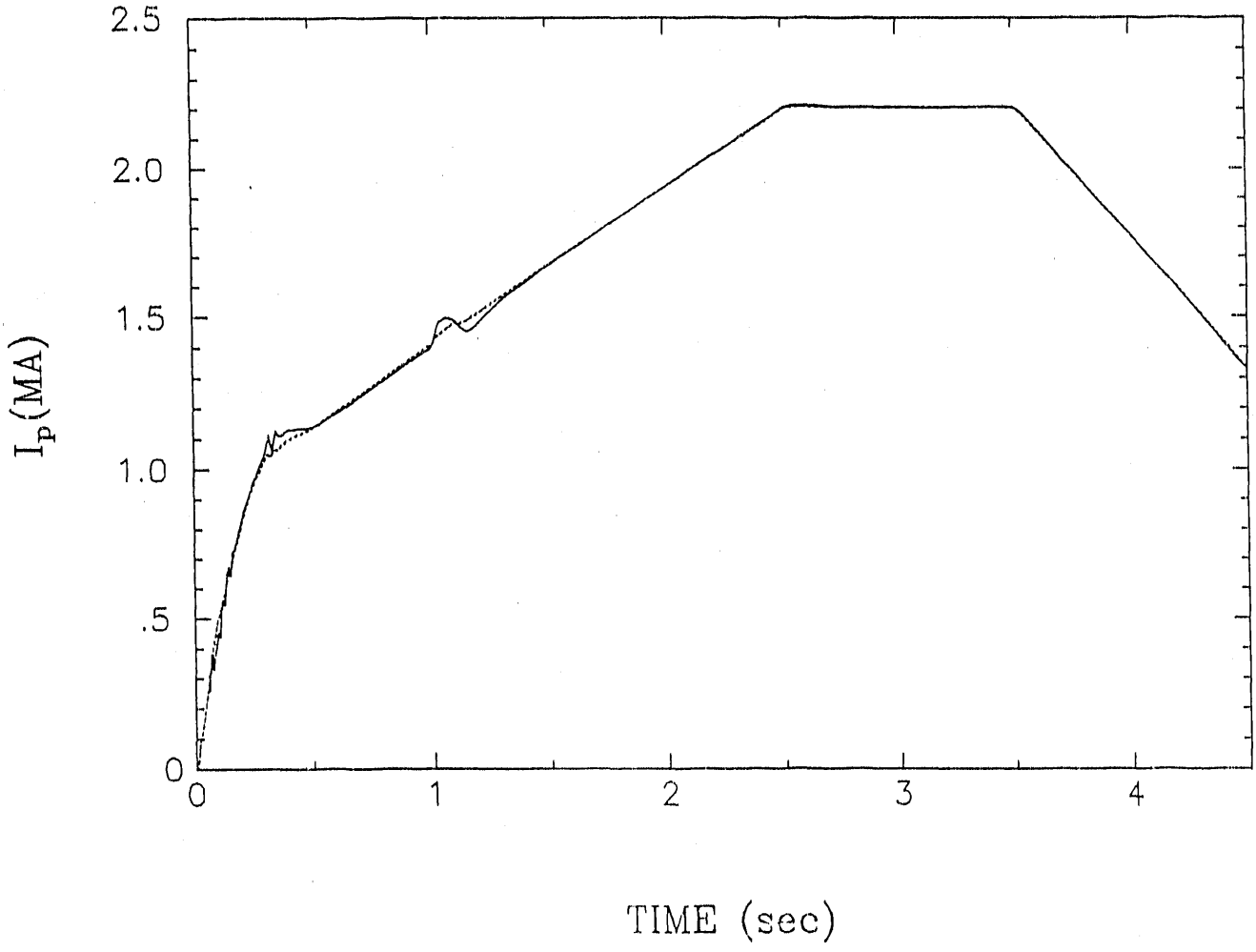

Fig. 1a

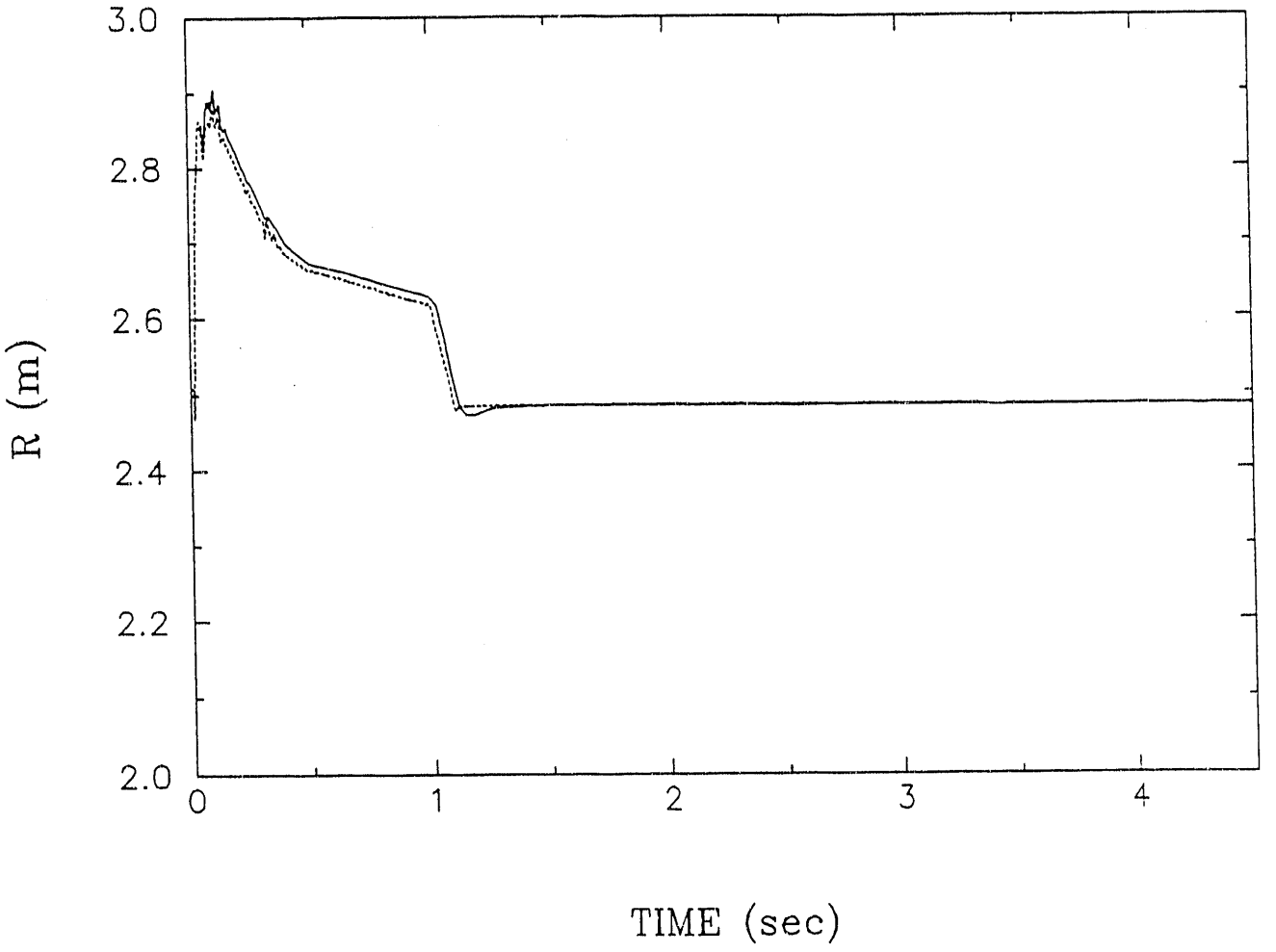

Fig. 1b

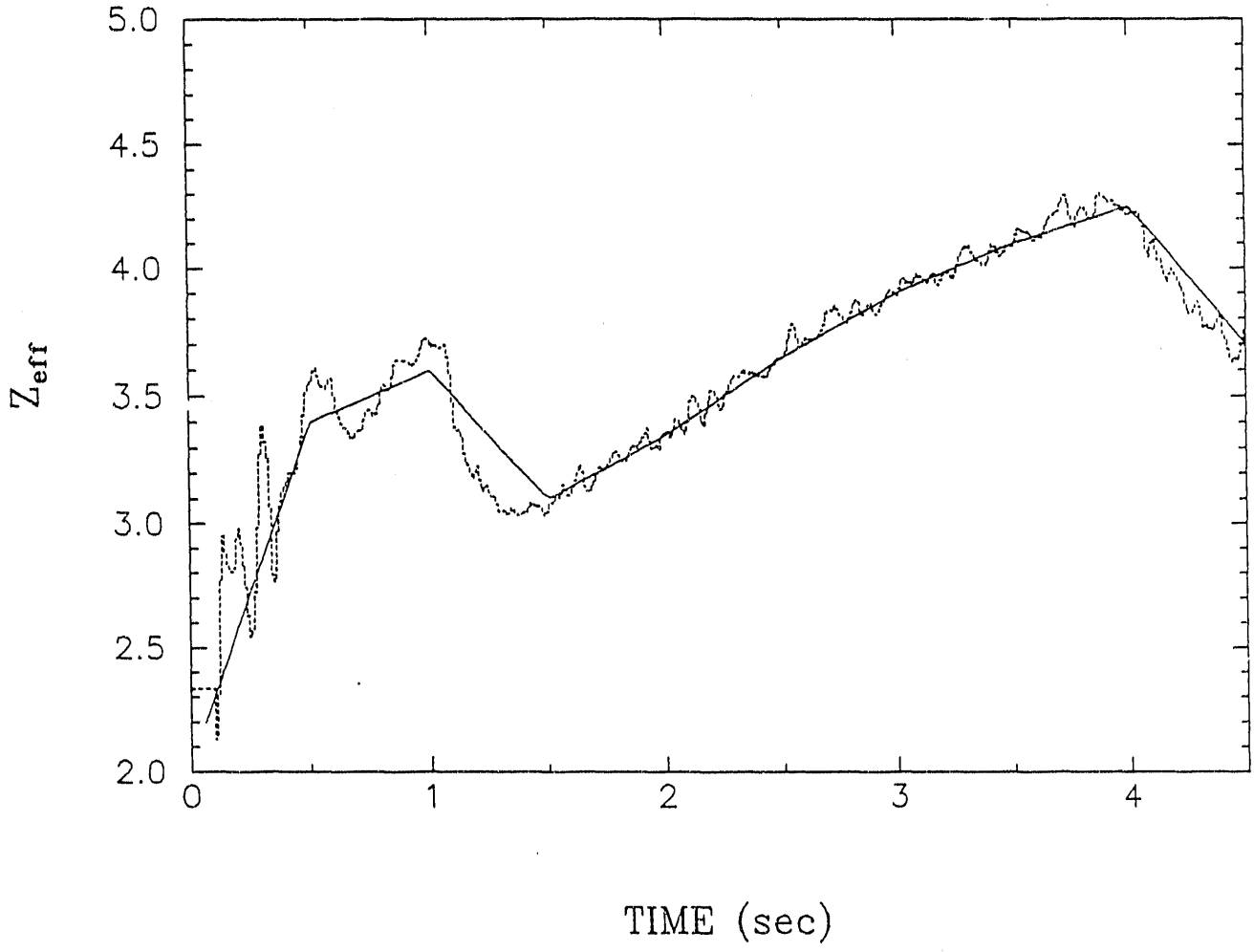

Fig. 2a

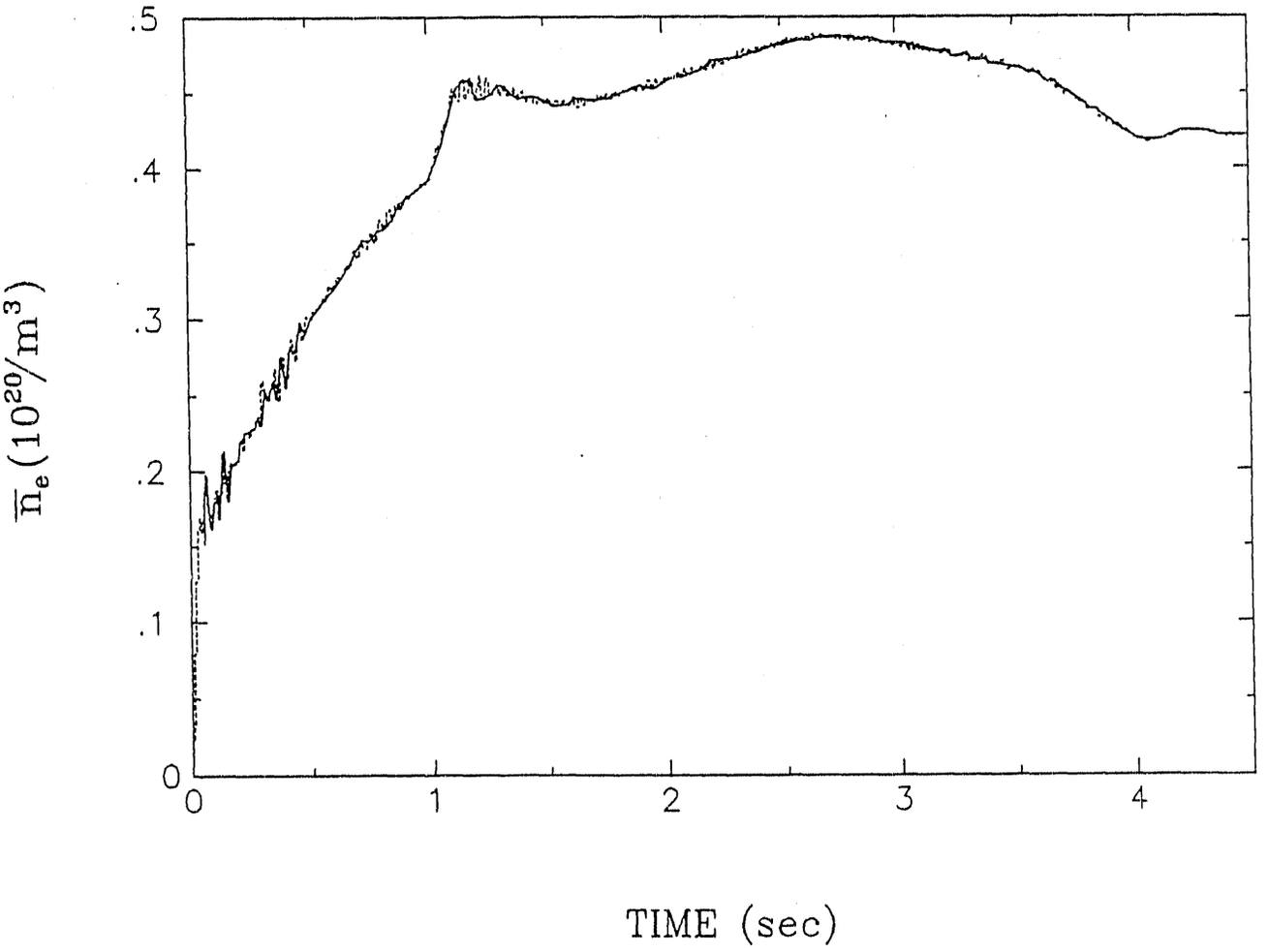

Fig. 2b

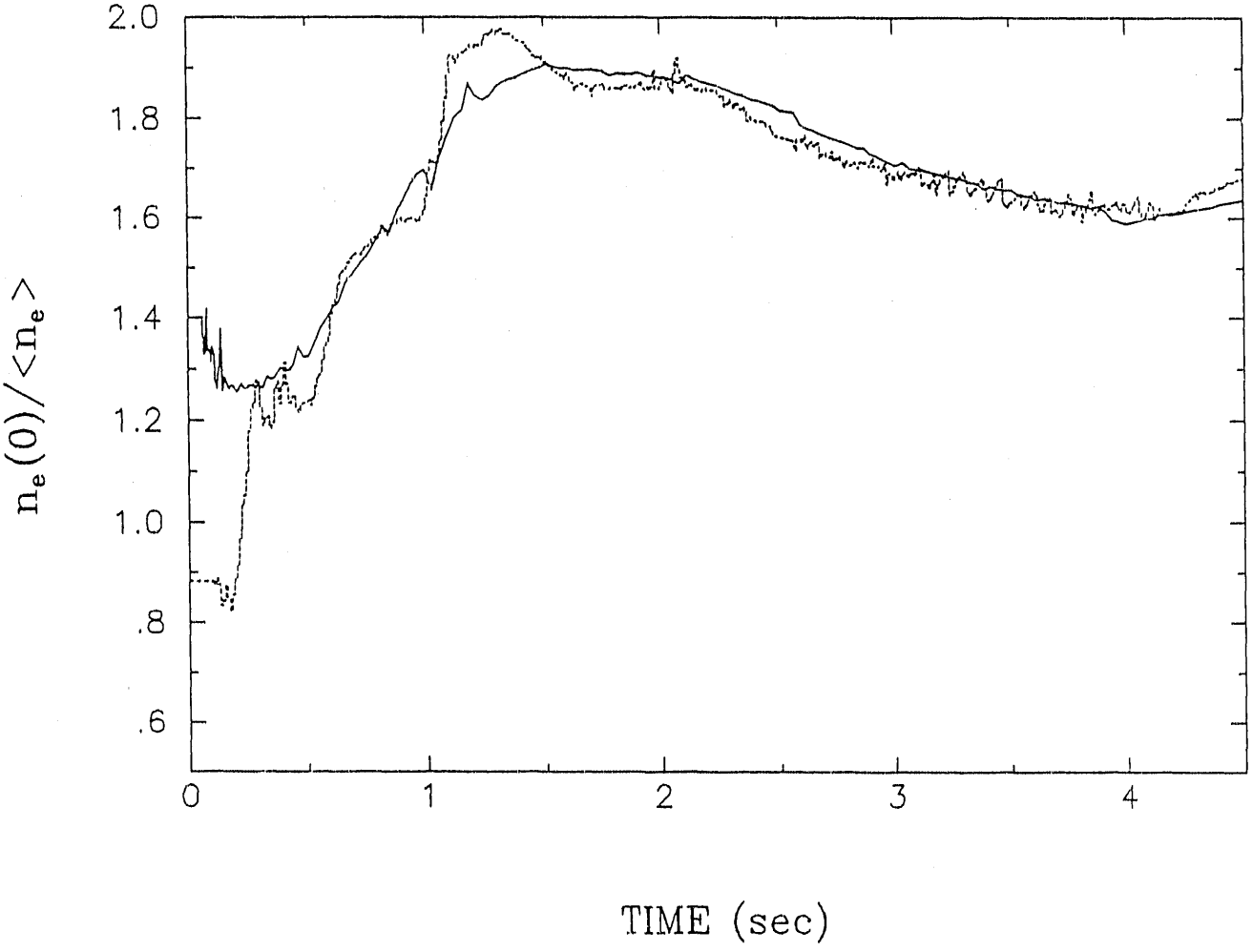

Fig. 2c

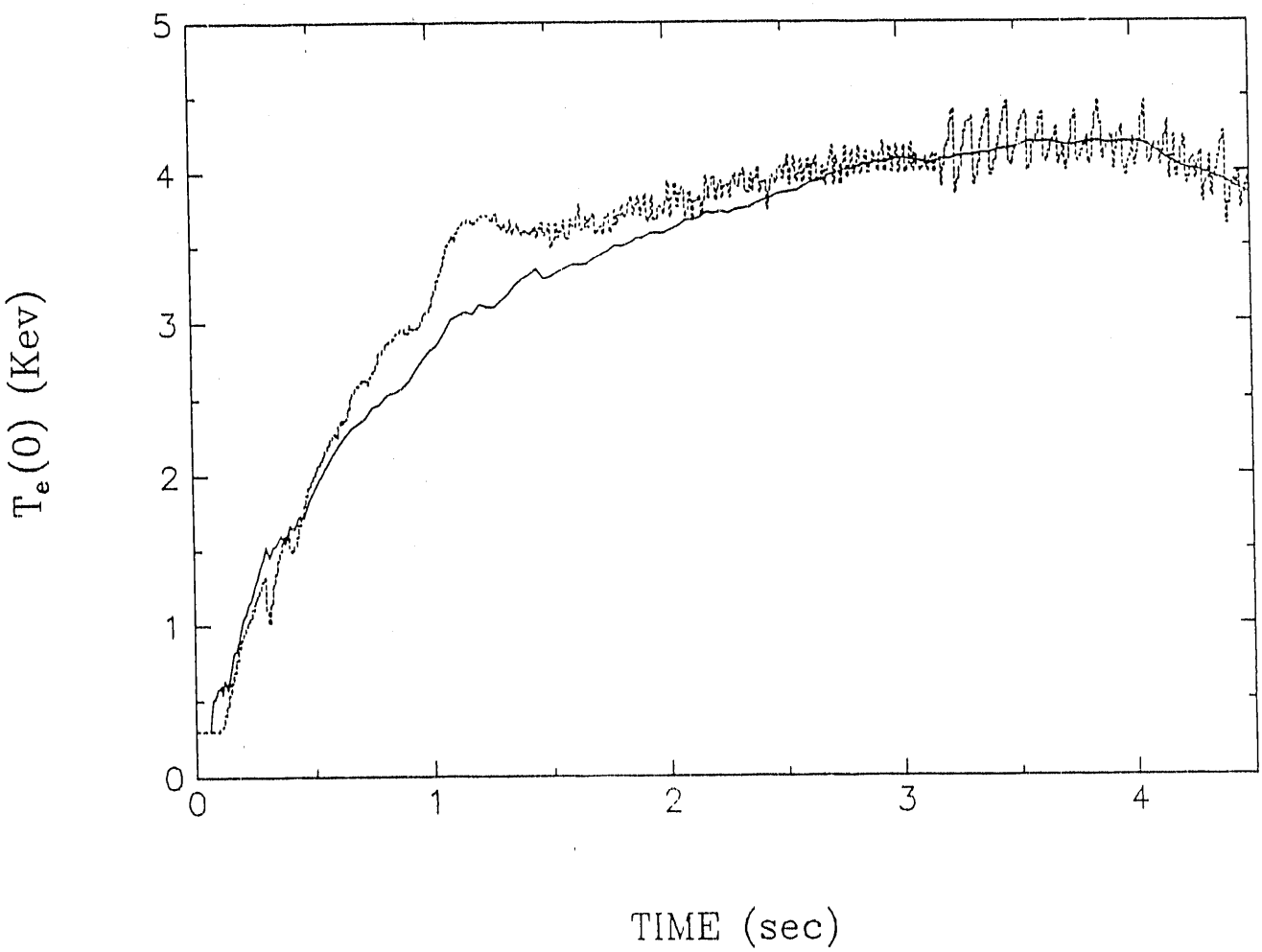

Fig. 3a

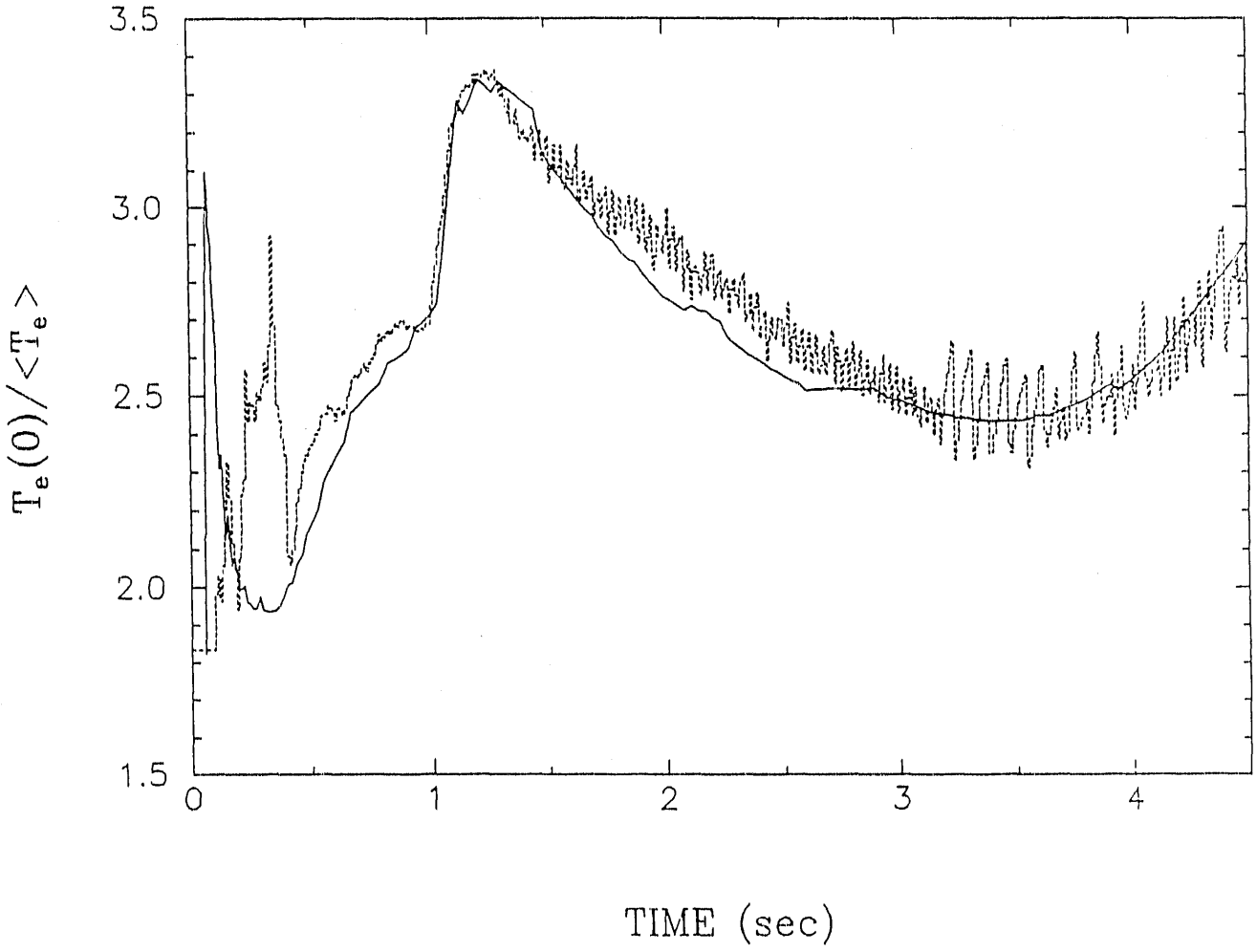

Fig. 3b

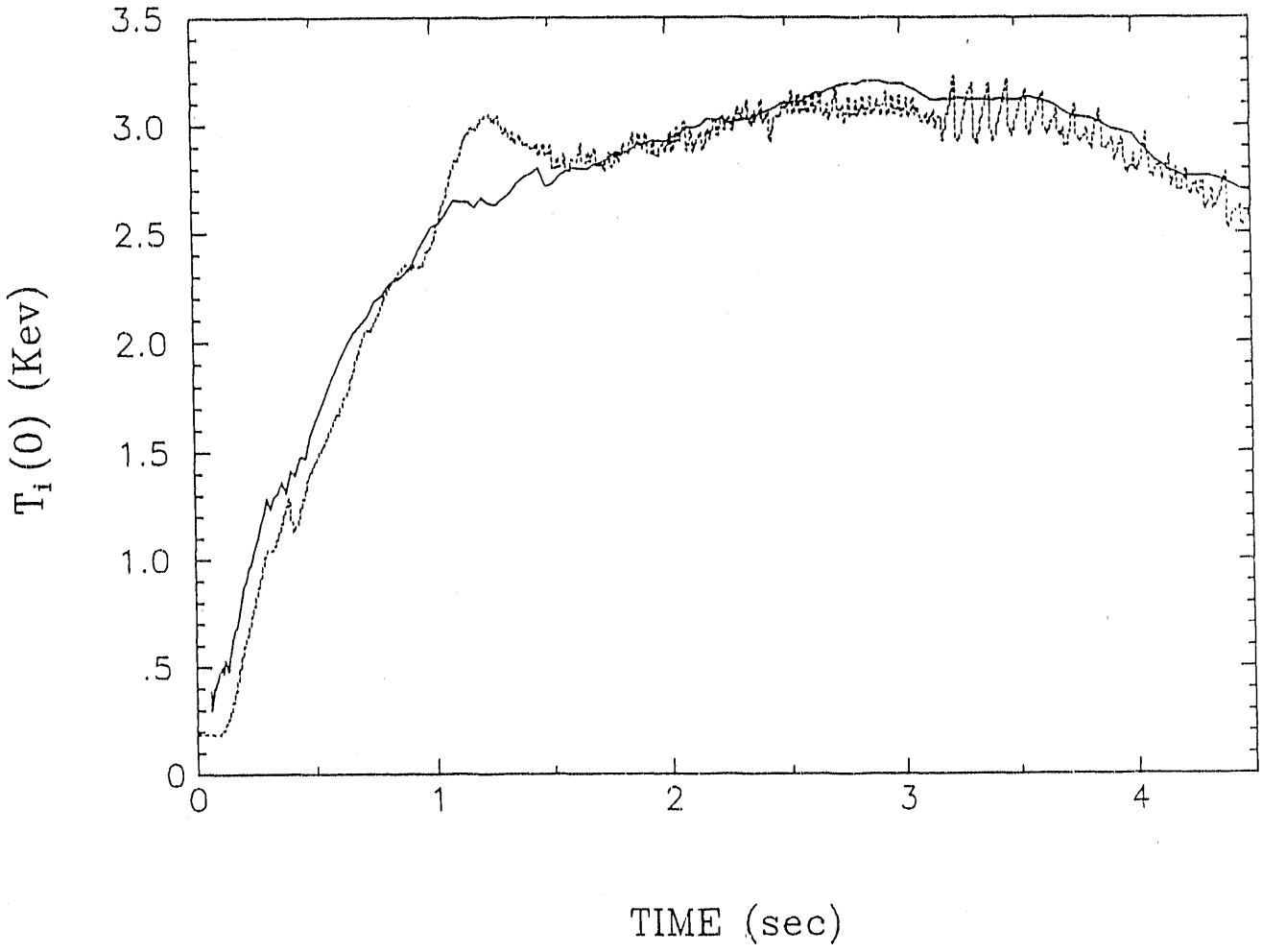

Fig. 4a

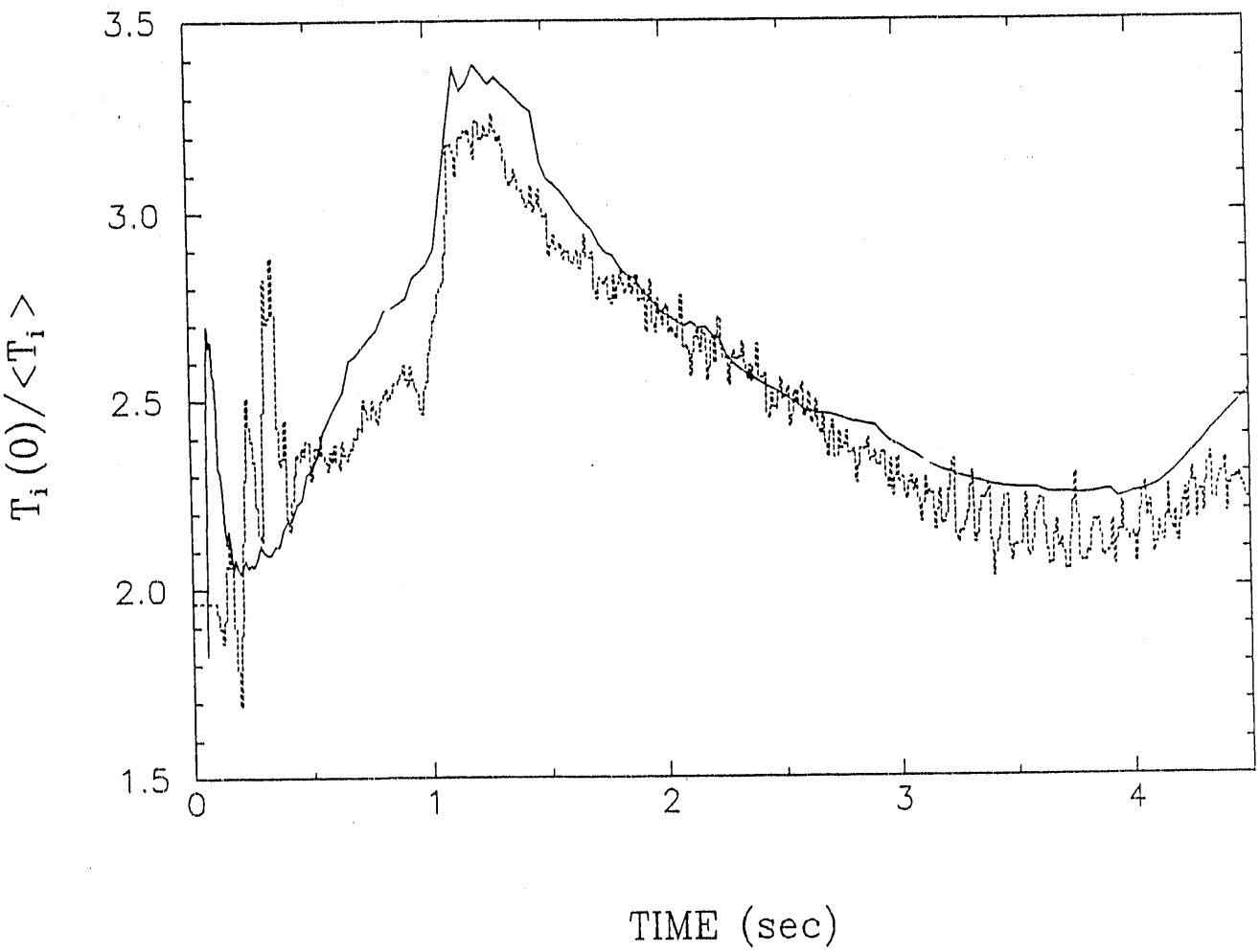

Fig. 4b

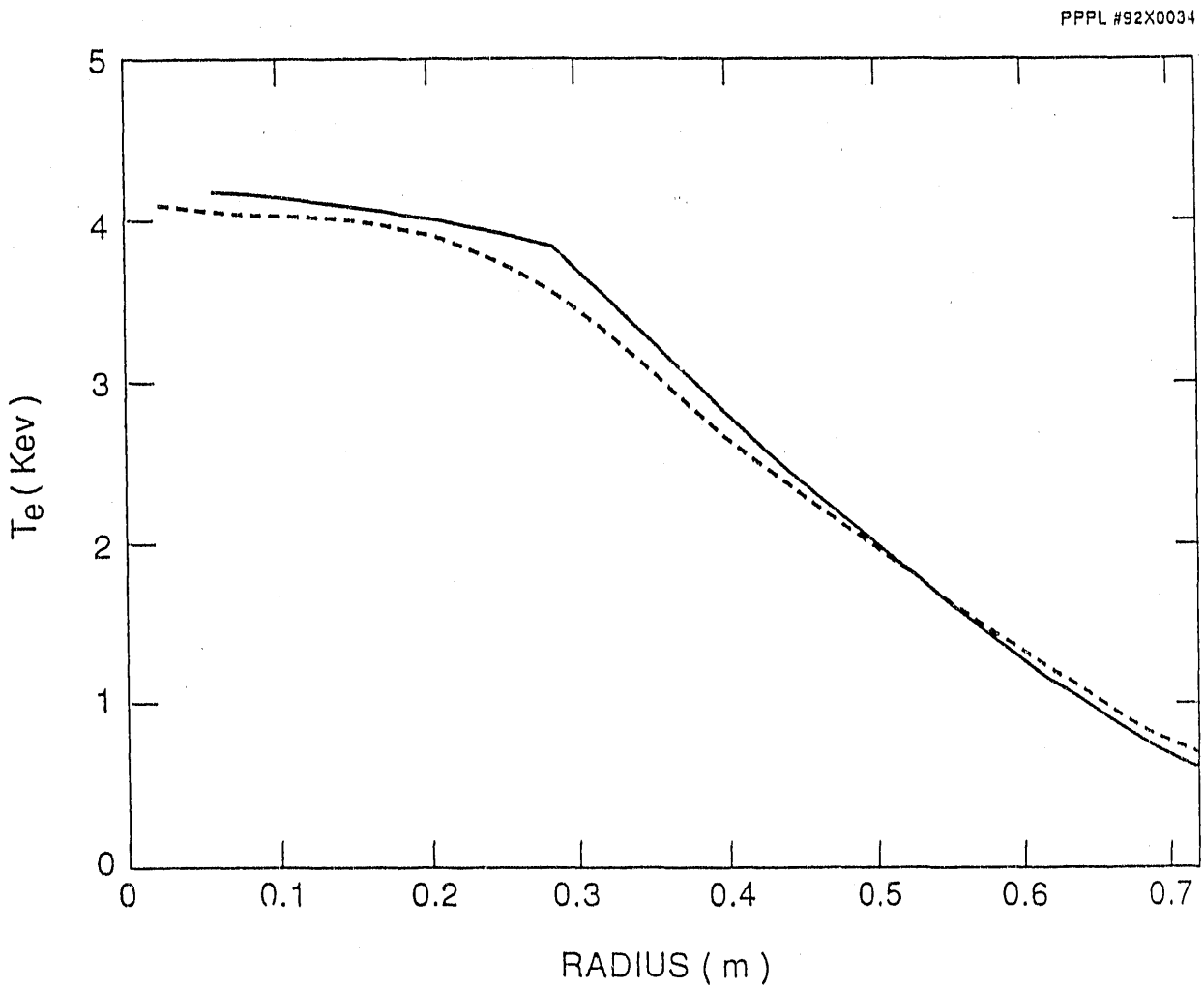

Fig. 5a

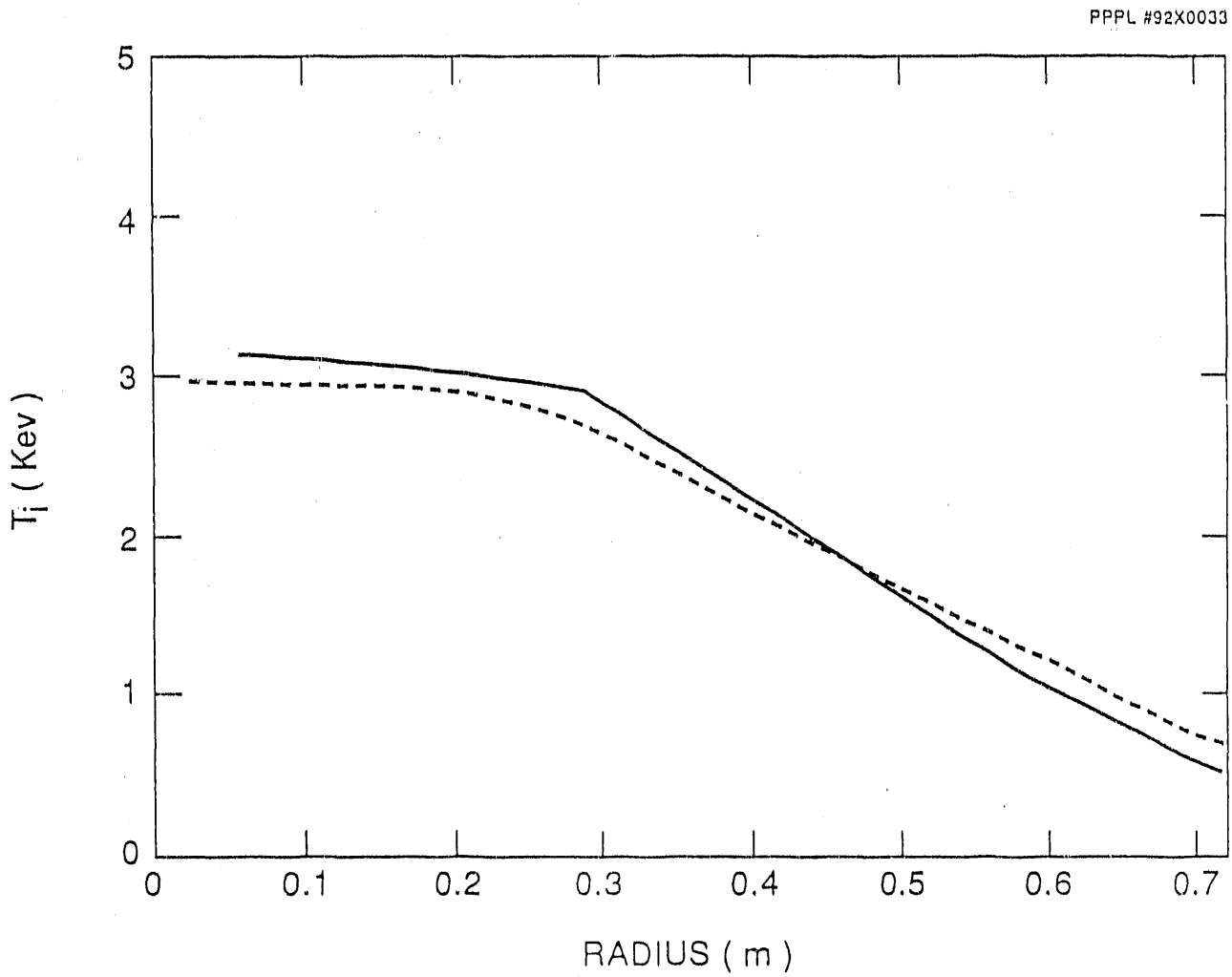

Fig. 5b

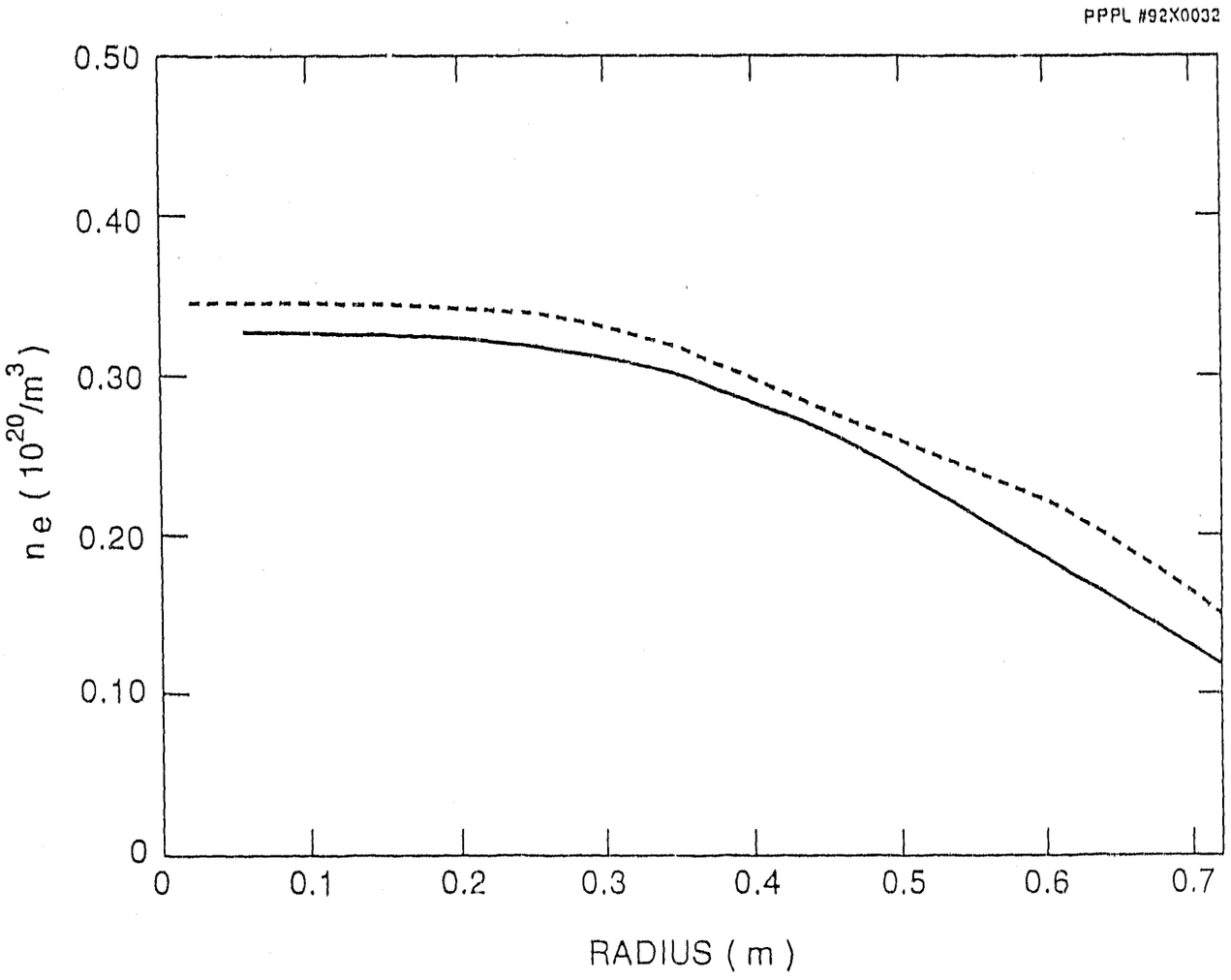
PPPL #92X0032
0.50
0.40
0.30
0.20
0.10
0
n e (10^20/m^3)
0
0.1
0.2
0.3
0.4
0.5
0.6
0.7
RADIUS (m)

Fig. 5c

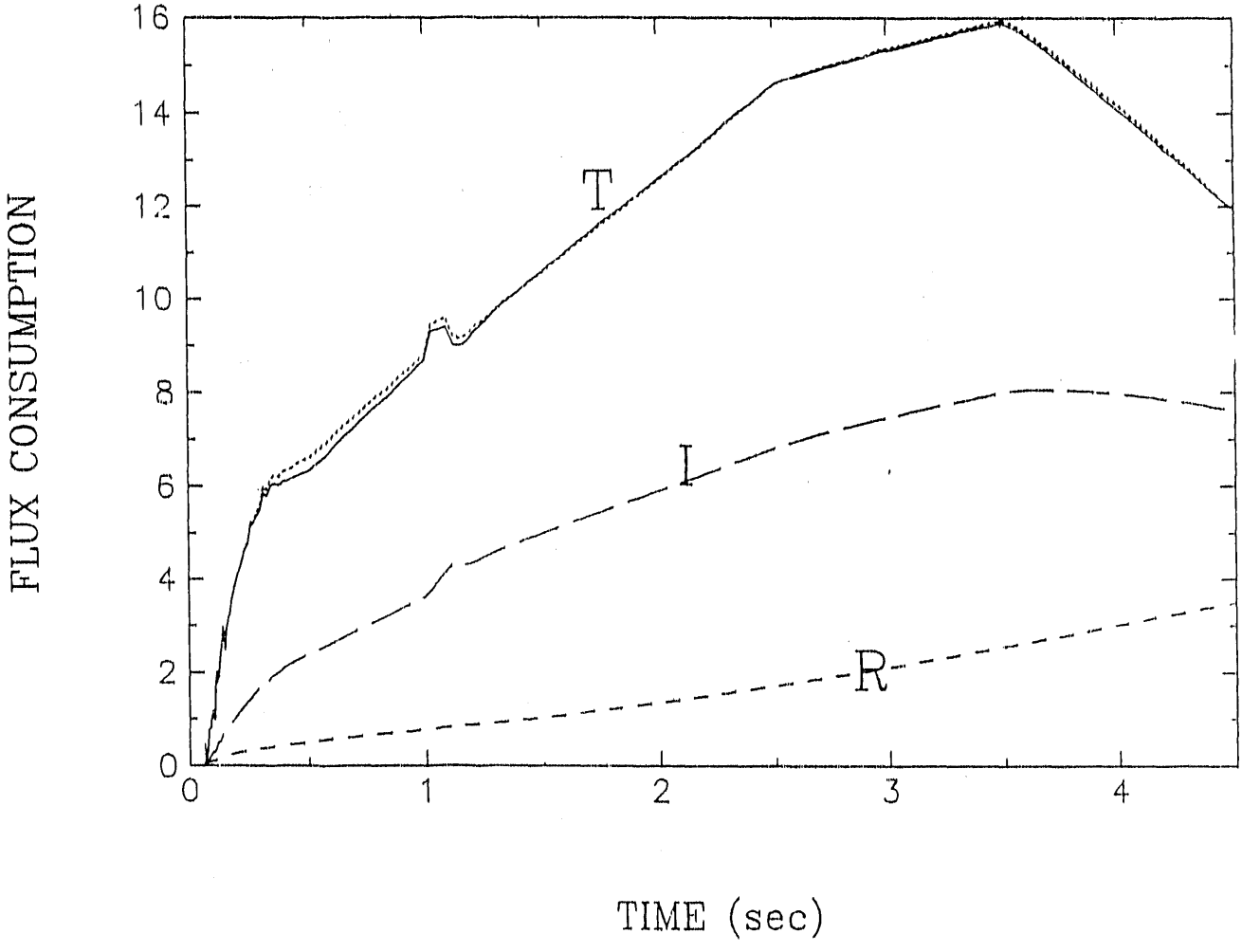

Fig. 6

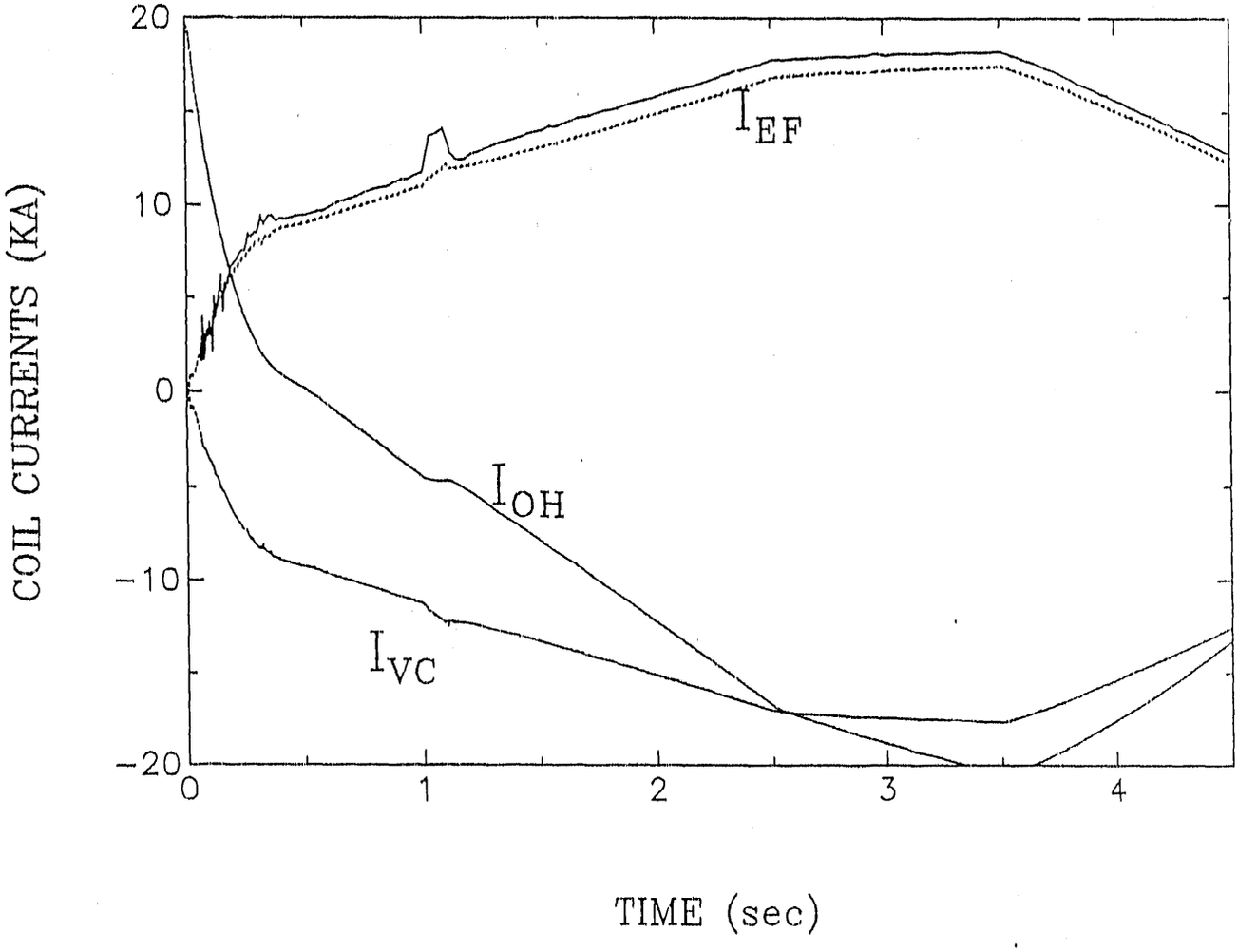

Fig. 7

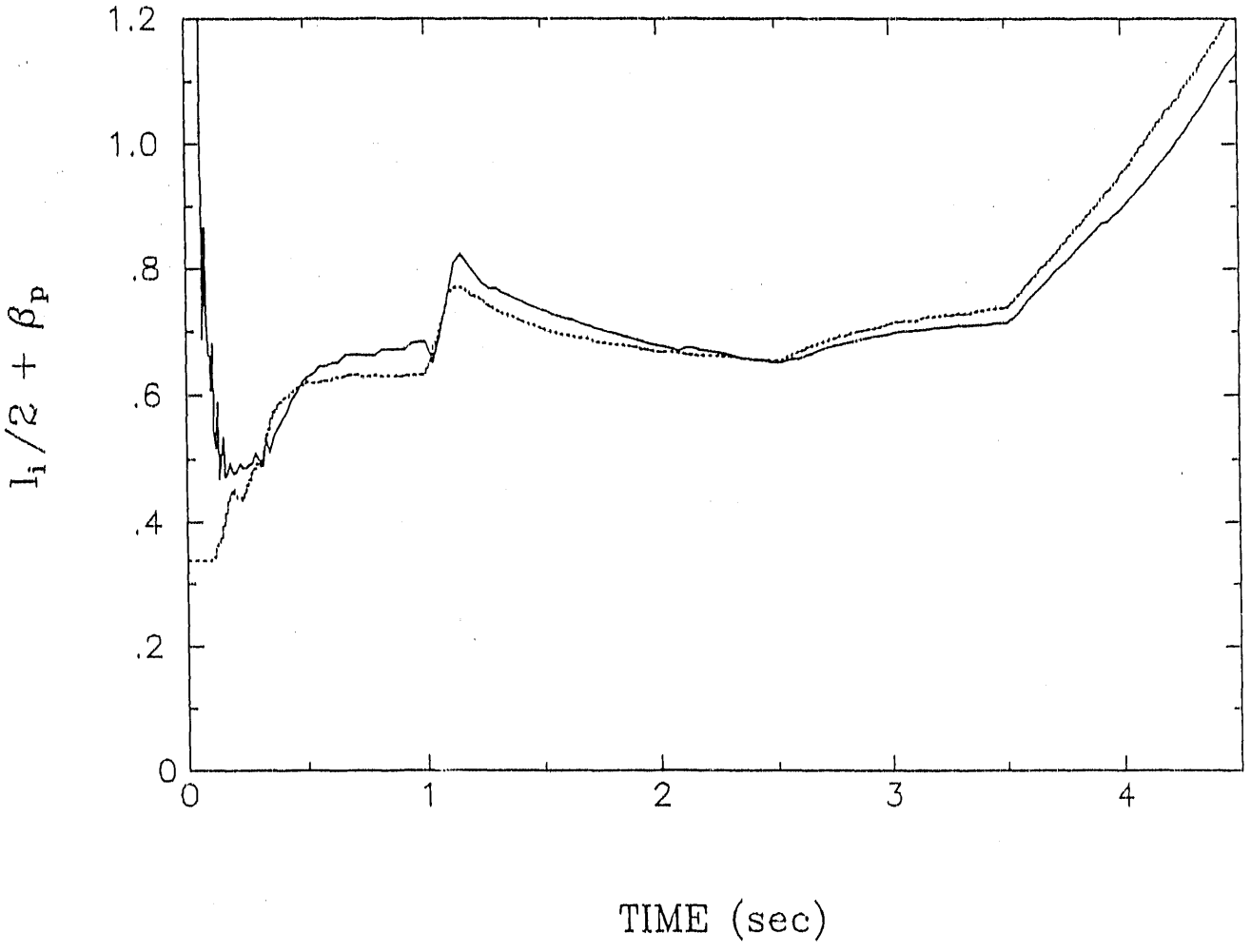

Fig. 8

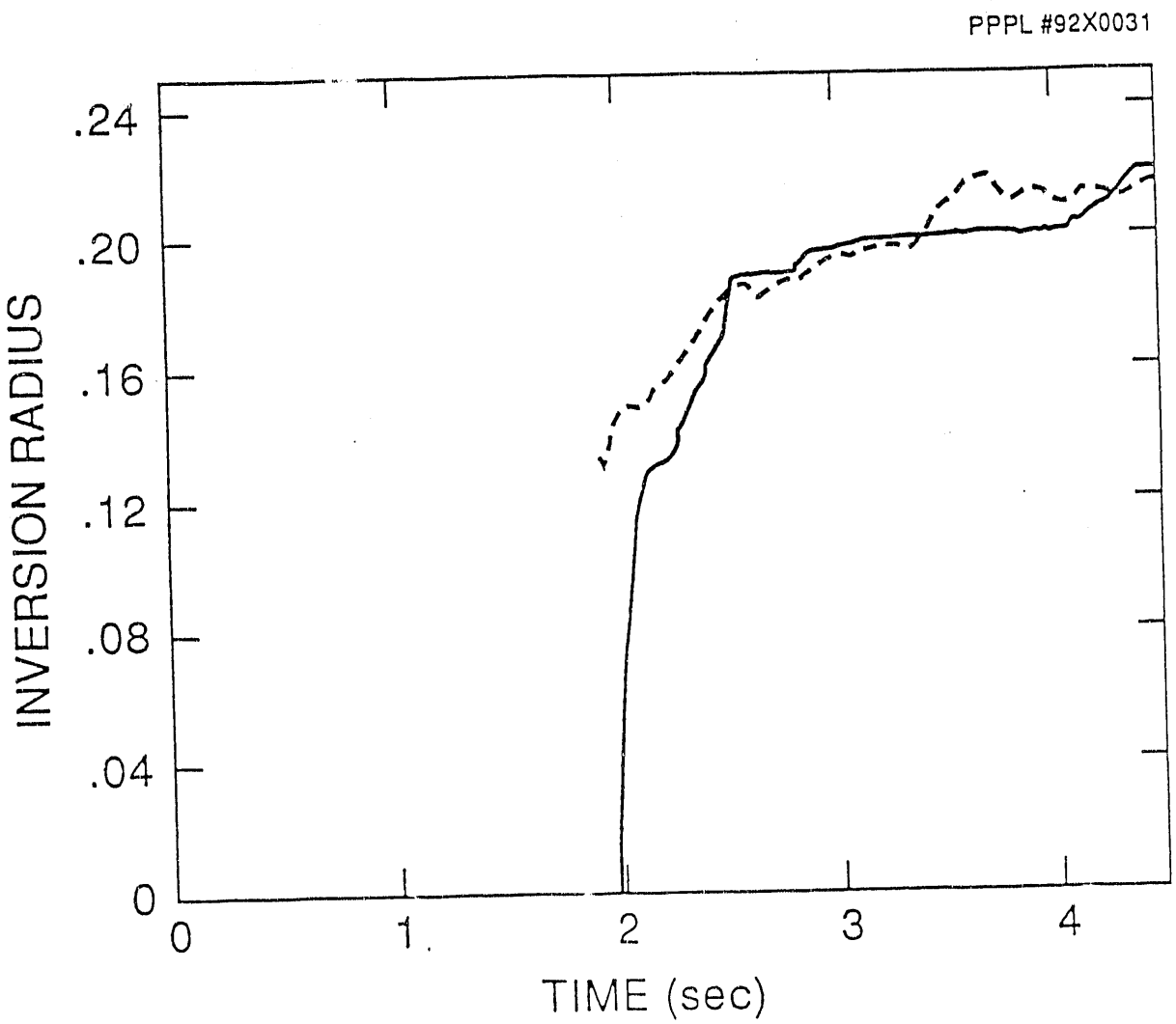
PPPL #92X0031
INVERSION RADIUS
.24
.20
.16
.12
.08
.04
0
0
1
2
3
4
TIME (sec)

Fig. 9

EXTERNAL DISTRIBUTION IN ADDITION TO UC-420

Dr. F. Paoloni, Univ. of Wollongong, AUSTRALIA
Prof. M.H. Brennan, Univ. of Sydney, AUSTRALIA
Plasma Research Lab., Australian Nat. Univ., AUSTRALIA
Prof. I.R. Jones, Flinders Univ, AUSTRALIA
Prof. F. Cap, Inst. for Theoretical Physics, AUSTRIA
Prof. M. Heindler, Institut für Theoretische Physik, AUSTRIA
Prof. M. Goossens, Astronomisch Instituut, BELGIUM
Ecole Royale Militaire, Lab. de Phy. Plasmas, BELGIUM
Commission-European, DG. XII-Fusion Prog., BELGIUM
Prof. R. Boucique, Rijksuniversiteit Gent, BELGIUM
Dr. P.H. Sakanaka, Instituto Fisica, BRAZIL
Instituto Nacional De Pesquisas Espaciais-INPE, BRAZIL
Documents Office, Atomic Energy of Canada Ltd., CANADA
Dr. M.P. Bachynski, MPB Technologies, Inc., CANADA
Dr. H.M. Skarsgard, Univ. of Saskatchewan, CANADA
Prof. J. Teichmann, Univ. of Montreal, CANADA
Prof. S.R. Sreenivasan, Univ. of Calgary, CANADA
Prof. T.W. Johnston, INRS-Energie, CANADA
Dr. R. Bolton, Centre canadien de fusion magnétique, CANADA
Dr. C.R. James,, Univ. of Alberta, CANADA
Dr. P. Lukác, Komenského Universzita, CZECHO-SLOVAKIA
The Librarian, Culham Laboratory, ENGLAND
Library, R61, Rutherford Appleton Laboratory, ENGLAND
Mrs. S.A. Hutchinson, JET Library, ENGLAND
Dr. S.C. Sharma, Univ. of South Pacific, FIJI ISLANDS
P. Mähönen, Univ. of Helsinki, FINLAND
Prof. M.N. Bussac, Ecole Polytechnique,, FRANCE
C. Mouttet, Lab. de Physique des Milieux Ionisés, FRANCE
J. Radet, CEN/CADARACHE - Bat 506, FRANCE
Prof. E. Economou, Univ. of Crete, GREECE
Ms. C. Rinni, Univ. of Ioannina, GREECE
Dr. T. Mual, Academy Bibliographic Ser., HONG KONG
Preprint Library, Hungarian Academy of Sci., HUNGARY
Dr. B. DasGupta, Saha Inst. of Nuclear Physics, INDIA
Dr. P. Kaw, Inst. for Plasma Research, INDIA
Dr. P. Rosenau, Israel Inst. of Technology, ISRAEL
Librarian, International Center for Theo Physics, ITALY
Miss C. De Palo, Associazione EURATOM-ENEA , ITALY
Dr. G. Grosso, Istituto di Fisica del Plasma, ITALY
Prof. G. Rostangni, Istituto Gas Ionizzati Del Cnr, ITALY
Dr. H. Yamato, Toshiba Res & Devel Center, JAPAN
Prof. I. Kawakami, Hiroshima Univ., JAPAN
Prof. K. Nishikawa, Hiroshima Univ., JAPAN
Director, Japan Atomic Energy Research Inst., JAPAN
Prof. S. Itoh, Kyushu Univ., JAPAN
Research Info. Ctr., National Instit. for Fusion Science, JAPAN
Prof. S. Tanaka, Kyoto Univ., JAPAN
Library, Kyoto Univ., JAPAN
Prof. N. Inoue, Univ. of Tokyo, JAPAN
Secretary, Plasma Section, Electrotechnical Lab., JAPAN
S. Mori, Technical Advisor, JAERI, JAPAN
Dr. O. Mitarai, Kumamoto Inst. of Technology, JAPAN
J. Hyeon-Sook, Korea Atomic Energy Research Inst., KOREA
D.I. Choi, The Korea Adv. Inst. of Sci. & Tech., KOREA
Prof. B.S. Liley, Univ. of Waikato, NEW ZEALAND
Inst of Physics, Chinese Acad Sci PEOPLE'S REP. OF CHINA
Library, Inst. of Plasma Physics, PEOPLE'S REP. OF CHINA
Tsinghua Univ. Library, PEOPLE'S REPUBLIC OF CHINA
Z. Li, S.W. Inst Physics, PEOPLE'S REPUBLIC OF CHINA
Prof. J.A.C. Cabral, Instituto Superior Tecnico, PORTUGAL
Dr. O. Petrus, AL I CUZA Univ., ROMANIA
Dr. J. de Villiers, Fusion Studies, AEC, S. AFRICA
Prof. M.A. Hellberg, Univ. of Natal, S. AFRICA
Prof. D.E. Kim, Pohang Inst. of Sci. & Tech., SO. KOREA
Prof. C.I.E.M.A.T, Fusion Division Library, SPAIN
Dr. L. Stenflo, Univ. of UMEA, SWEDEN
Library, Royal Inst. of Technology, SWEDEN
Prof. H. Wilhelmson, Chalmers Univ. of Tech., SWEDEN
Centre Phys. Des Plasmas, Ecole Polytech, SWITZERLAND
Bibliotheek, Inst. Voor Plasma-Fysica, THE NETHERLANDS
Asst. Prof. Dr. S. Cakir, Middle East Tech. Univ., TURKEY
Dr. V.A. Glukhikh,Sci. Res. Inst. Electrophys.I Apparatus, USSR
Dr. D.D. Ryutov, Siberian Branch of Academy of Sci., USSR
Dr. G.A. Eliseev, I.V. Kurchatov Inst., USSR
Librarian, The Ukr.SSR Academy of Sciences, USSR
Dr. L.M. Kovrizhnykh, Inst. of General Physics, USSR
Kernforschungsanlage GmbH, Zentralbibliothek, W. GERMANY
Bibliothek, Inst. Für Plasmaforschung, W. GERMANY
Prof. K. Schindler, Ruhr-Universität Bochum, W. GERMANY
Dr. F. Wagner, (ASDEX), Max-Planck-Institut, W. GERMANY
Librarian, Max-Planck-Institut, W. GERMANY
Prof. R.K. Janev, Inst. of Physics, YUGOSLAVIA

END

DATE
FILMED
6/12/92